# A Numerical Handling of the Boundary Conditions Imposed by the Skull on an Inhomogeneous Diffusion-Reaction Model of Glioblastoma Invasion Into the Brain: Clinical Validation Aspects

Cancer Informatics
1–16

DOI: 10.1177/1176935116684824

Georgios S Stamatakos and Stavroula G Giatili

*In Silico* Oncology and *In Silico* Medicine Group, Institute of Communication and Computer Systems, National Technical University of Athens, Zografou, Greece.

**ABSTRACT:** A novel explicit triscale reaction-diffusion numerical model of glioblastoma multiforme tumor growth is presented. The model incorporates the handling of Neumann boundary conditions imposed by the cranium and takes into account both the inhomogeneous nature of human brain and the complexity of the skull geometry. The finite-difference time-domain method is adopted. To demonstrate the workflow of a possible clinical validation procedure, a clinical case/scenario is addressed. A good agreement of the *in silico* calculated value of the doubling time (ie, the time for tumor volume to double) with the value of the same quantity based on tomographic imaging data has been observed. A theoretical exploration suggests that a rough but still quite informative value of the doubling time may be calculated based on a homogeneous brain model. The model could serve as the main component of a continuous mathematics-based glioblastoma oncosimulator aiming at supporting the clinician in the optimal patient-individualized design of treatment using the patient's multiscale data and experimenting *in silico* (ie, on the computer).

**KEYWORDS:** boundary value problem, diffusion, glioblastoma multiforme, inhomogeneous, *in silico* oncology, multiscale cancer modeling, tumor growth

**RECEIVED:** April 2, 2016. **ACCEPTED:** November 24, 2016.

**PEER REVIEW:** Seven peer reviewers contributed to the peer review report. Reviewers' reports totaled 1662 words, excluding any confidential comments to the academic editor.

**TYPE:** Original Research

**FUNDING:** The author(s) disclosed receipt of the following financial support for the research, authorship, and/or publication of this article: This work has been supported in part by the European Commission in the framework the projects "p-Medicine: Personalized Medicine (FP7-ICT-2009.5.3-270089)," "CHIC—Computational Horizons in Cancer (CHIC): Developing Meta- and Hyper-Multiscale Models and Repositories for *In Silico* Oncology" (FP7-ICT-2011-9-600841), MyHealthAvatar (PI: 600929), and DR THERAPAT (PI: 600852).

**DECLARATION OF CONFLICTING INTERESTS:** The author(s) declared no potential conflicts of interest with respect to the research, authorship, and/or publication of this article.

**CORRESPONDING AUTHOR:** Georgios S Stamatakos, *In Silico* Oncology and *In Silico* Medicine Group, Institute of Communication and Computer Systems, National Technical University of Athens, 9 Iroon Polytechniou, GR-157 80 Zografou, Greece. Email: gestam@central.ntua.gr

## Introduction

Gliomas are the most common type of primary intracranial tumor. They represent 81% of malignant brain and central nervous system tumors.[1] Glioblastoma multiforme (GBM) accounts for roughly 75% of all high-grade gliomas[2] and represents the most aggressive subgroup of malignant gliomas, with a median survival of 6 months following surgical resection alone and about 14 to 17 months in patients who undergo the most aggressive combined modality treatments.[3] Principles of treatment revolve around cytoreduction via multimodality treatment: surgical resection, radiation, and chemotherapy. These survival rates are to be correlated with systematic relapses that might arise from remaining glioblastoma stem cells left behind after surgery.[4] Glioblastomas nearly always recur near the resection cavity or radiotherapy volume; a small percentage recur more distantly.[5]

Magnetic resonance imaging (MRI) is the current clinical criterion standard for the assessment of intracranial pathology, but it is limited by the fact that the origins of its signal are merely surrogate markers of tumor presence.[2] A considerable part of GBM cells diffused within a large volume of the brain are not tomographically imageable. Tissue invasion is a hallmark of most human cancers and remains a major source of treatment failure in patients with glioblastoma (GBM).[6] Glioblastoma multiforme is one of the most diffusive and invasive cancers in humans.

Crucial aspects of the interaction of cancer cells with the host being locally represented by several microscopic structures are taken into account in the model presented. Glioblastoma cell migration is greater in white than in gray matter, and the proposed model accounts for cell diffusion into the cerebrospinal fluid (CSF) even though it appears that tumor cells rarely enter the CSF.[5] Invading glioma cells seem to follow distinct anatomic structures within the central nervous system. Tumor cell dissemination may occur along structures, such as the basement membranes of blood vessels or the glial limitans externa, that contain extracellular matrix proteins. Frequently, invasive glioma cells are also found to migrate along myelinated fiber tracts of white matter. This behavior is most likely a consequence of using constitutive extracellular ligands expressed along the pathways of preferred dissemination.[7]

For an accurate and reliable simulation outcome, consideration of the actual physical boundary of the cranium is important. An improper handling of the boundary conditions may lead to an unnatural behavior of the simulated system. The process of understanding the phenomenon of diffusion-invasion taking place inside the brain has attracted

considerable attention by researchers because it may have important therapeutic implications. In this context, 2 major cancer modeling schools of thought have developed. The continuous entity school of thought largely adopts the diffusion-reaction equation at its core.[8–26] The discrete entity-discrete event school of thought relies on the use of discrete constructs, such as cellular automata, and considers discrete mitotic potential cell categories, discrete phases of the cell cycle, and differing radiosensitivities and chemosensitivities.[27–34] A combination of both mathematical approaches would eventually lead to a better understanding of both glioma invasion and its response to treatment even in the context of complex experimental therapies.

The practical goal of this work is to develop a "bottom-up" multiscale (triscale) mathematical model of glioma growth and invasion that would serve as the core of the "continuous mathematics-based GBM Oncosimulator." The triscale character of the model refers to the concurrent consideration of the cell scale (tumor cell birth and death rates, tumor cell diffusion coefficient), the tissue scale (white matter, gray matter, CSF, bone), and the organ scale (brain, skull). The purpose of the oncosimulator is to simulate, investigate, better understand, and explore the natural phenomenon of tumor growth and response to treatment. Following a rigorous clinical validation, the oncosimulator under discussion is meant to support the clinician in patient-specific tailoring and optimizing cancer treatment through *in silico* (ie, on the computer) experimentation.

From the mathematical perspective, tumor growth and invasion of cancer cells into the surrounding tissue can be described as a boundary value problem which strongly depends on the actual values assigned on the physical boundary of the domain in which the problem is defined. This article provides a synthesis and extension of previous efforts[35] concerning the numerical treatment of the adiabatic Neumann boundary conditions imposed by the physical boundary of cranium on the growth of GBM. The main theme of the article is the numerical handling of the diffusion-reaction equation applied on an inhomogeneous model of brain subject to Neumann boundary conditions for which an explicit numerical treatment is provided (section "Materials and Methods—Mathematical Model"). The Crank-Nicolson method in conjunction with the biconjugate gradient BiCG system solver is used. Several *in silico* experiments are conducted for validity checking purposes referring to both the numerical method and the model and illustrate the practical applicability of both (section "Generic Error Estimation Checks"). Good qualitative and even semiquantitative agreements between the simulated and the clinically manifested courses of the disease have been observed and are presented in section "Numerical Experiments." The concept of tumor volume doubling time, $T_d$, which is defined as the time for the tumor volume to double,[36] is widely used for quantification of the growth rate of a tumor. The potential of the model and the next planned steps are discussed in section "Discussion."

## Materials and Methods—Mathematical Model

Glioblastoma multiforme cell invasion into the brain appears to follow the general reaction-diffusion law. The related diffusion phenomena can be described by Fick's second law of diffusion, which is mathematically expressed in the form of a second-order partial differential equation, generally referred to as the diffusion equation. Tumor growth and invasion including the effect of treatment can be expressed by the following statement[37,38]:

Rate of tumor cell population change = tumor cell diffusion(motility) + tumor cell net proliferation − tumor cell loss due to treatment

The boundary value problem under consideration can be expressed by a differential equation in conjunction with a set of additional constraints, the boundary conditions. A solution to a boundary value problem is a solution to the differential equation which also satisfies the boundary conditions. The region of interest in our case may include part of or the cranium. In the 3-dimensional (3D) case of GBM, the skull acts as an adiabatic boundary for the diffusion of the tumor. The Neumann boundary conditions corresponding to no net flow of tumor cells out of or into the brain region across the brain-skull boundary have been adopted. In the simplest case of 1-dimensional problem, the formulation described in a study by Sharma et al[39] has been proposed. Thus, if $\Omega$ is the brain domain, the previous statement can be translated into the following differential equation[8(pp536–613)]:

$$\frac{\partial c(x,y,z,t)}{\partial t} = \nabla \cdot \left[ D(x,y,z) \nabla c(x,y,z,t) \right] + \rho c(x,y,z,t) - G(t) c(x,y,z,t) \text{ in } \Omega \quad (1)$$

with the initial condition

$$c(x,y,z,0) = f(x,y,z) \quad (2)$$

and the Neumann boundary condition

$$\hat{n} \cdot D(x,y,z) \nabla c(x,y,z,t) = 0 \text{ on } \partial\Omega \quad (3)$$

The parameter $c$ stands for the cell concentration at time $t$ and at any spatial point $\vec{x} = (x,y,z)$. The term $\rho$ represents the net tumor growth rate which includes cell proliferation, cell loss, and cell death. The latter includes cell loss due to spontaneous apoptosis and necrosis induced by the lack of oxygen and nutrient provision. The unit normal vector on the surface of the boundary $\partial\Omega$ of the domain $\Omega$ is denoted by $\hat{n}$. The term $f$ stands for a known function expressing the initial spatial distribution of glioma cells. The term $G(t)$ denotes the temporal profile of treatment (eg, chemotherapy, radiotherapy, targeted therapies, and combined therapies) and as a first approximation is assumed to be constant. The brain domain is a subdomain of the simulation domain $R$, which is defined as follows:

$$R = \left\{ \vec{x} \,|\, a < x < b, s < y < d, e < z < f \right\}. \quad (4)$$

The diffusion coefficient $D$ is a measure of the active motility of glioma cells which depends on position. In the inhomogeneous case where the diffusion coefficient is a de facto function of position, 3 kinds of $D$ have been considered depending on the local structure of the human brain (Figure 1): the diffusion coefficient $D_g$ if $(\vec{x}) = (x, y, z)$ pertaining to gray matter, the diffusion coefficient $D_w$ if $(x, y, z)$ pertaining to white matter, and the diffusion coefficient $D_{CSF}$ if $(x, y, z)$ pertaining to CSF:

$$D(x, y, z) = \left\{ \begin{array}{c} D_g \text{ for } (\vec{x}) \text{ in grey matter} \\ D_w \text{ for } (\vec{x}) \text{ in white matter} \\ D_{CSF} \text{ for } (\vec{x}) \text{ in } CSF \end{array} \right\} \quad (5)$$

In diffusing gliomas, tumor cells preferentially invade along myelinated fibers in white matter tracts. For this reason, diffusion in white matter has been set to a value greater than its counterpart in gray matter. In the clinical GBM case where a space-dependent diffusion coefficient is involved (inhomogeneous diffusion), closed-form solutions are not available, and therefore, resorting to a numerical solution of the diffusion-reaction equation is mandatory. To this end, the finite-difference method has been recruited. The involvement of the spatially variable diffusion coefficient $D$ leads to the following expression of the general form of equations (1), (2), and (3):

$$\begin{aligned} \frac{\partial c(x, y, z, t)}{\partial t} = & \left( \nabla D(x, y, z) \right) \cdot \left( \nabla c(x, y, z, t) \right) + \\ & D(x, y, z) \left( \nabla^2 c(x, y, z, t) \right) + \\ & \rho c(x, y, z, t) - G(t) c(x, y, z, t) \text{ in } \Omega \end{aligned} \quad (6)$$

with the initial condition

$$c(x, y, z, 0) = f(x, y, z) \quad (7)$$

and the Neumann boundary condition

$$\hat{n} \cdot D(x, y, z) \nabla c(x, y, z, t) = 0 \text{ on } \partial\Omega \quad (8)$$

It is noted that the boundaries between the white and the gray matter are not ideally sharp due to the interweaving between the cellular structures of the 2 matters and the gradual transition from gray matter to white matter, and vice versa. The spatial discretization of the problem, partly dictated by the actual digital tomographic data, leads to a noncontinuous and subsequently a nonstrictly differentiable $D$ function. But calculating derivatives in discrete meshes under such circumstances is an important part of numerical analysis.

A system of Cartesian coordinates and a cubic discretization grid have been selected for the simulation domain. The differentials involved have been discretized on the computational mesh

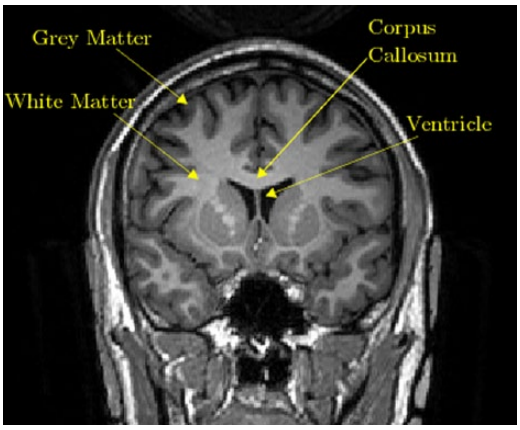


**Figure 1.** T1-weighted magnetic resonance image of a coronal section through the brain. Gray matter and white matter are indicated, as well as the ventricles and the corpus callosum.
Adapted with permission from Fieremans.[40]

of space and time. It is noted that the skull geometry is very complicated. Cartesian grids may not capture such geometry very accurately. For example, the boundary may have a zigzag shape. Subsequently, a Cartesian grid may bring some errors into the simulation. However, due to the fact that the available imaging data make use of Cartesian grids of which the elementary voxel is of the order of 1 mm$^3$ (equal to the voxel dimensions adopted in the numerical treatment executions), adoption of a Cartesian grid is a plausible and realistic approach to the discretization of the problem. Having defined the computational grid, equations (6), (7), and (8) can be rewritten equivalently as follows:

$$\begin{aligned} \frac{\partial c}{\partial t} = & \left( \frac{\partial D}{\partial x}\hat{i} + \frac{\partial D}{\partial y}\hat{j} + \frac{\partial D}{\partial z}\hat{k} \right) \cdot \left( \frac{\partial c}{\partial x}\hat{i} + \frac{\partial c}{\partial y}\hat{j} + \frac{\partial c}{\partial z}\hat{k} \right) + \\ & D\left( \frac{\partial^2 c}{\partial x^2} + \frac{\partial^2 c}{\partial y^2} + \frac{\partial^2 c}{\partial z^2} \right) + \rho c - G(t) c \text{ in } \Omega \end{aligned} \quad (9)$$

with the initial condition

$$c(x, y, z, 0) = f(x, y, z) \quad (10)$$

and the boundary condition

$$\hat{n} \cdot D(x, y, z) \left( \frac{\partial c}{\partial x}\hat{i} + \frac{\partial c}{\partial y}\hat{j} + \frac{\partial c}{\partial z}\hat{k} \right) = 0 \text{ on } \partial\Omega \quad (11)$$

Applying the Crank-Nicolson scheme[41] leads to

$$\frac{\partial c}{\partial t} \to \frac{c_{i,j,k}^{t+1} - c_{i,j,k}^{t}}{\Delta t} \quad (12)$$

$$\frac{\partial c}{\partial x} \to \frac{1}{2} \left( \frac{c_{i+1,j,k}^{t+1} - c_{i-1,j,k}^{t+1}}{2\Delta x} + \frac{c_{i+1,j,k}^{t} - c_{i-1,j,k}^{t}}{2\Delta x} \right) \quad (13)$$

$$\frac{\partial c}{\partial y} \to \frac{1}{2} \left( \frac{c_{i,j+1,k}^{t+1} - c_{i,j-1,k}^{t+1}}{2\Delta y} + \frac{c_{i,j+1,k}^{t} - c_{i,j-1,k}^{t}}{2\Delta y} \right) \quad (14)$$

$$\frac{\partial c}{\partial z} \to \frac{1}{2}\left( \frac{c_{i,j,k+1}^{t+1} - c_{i,j,k-1}^{t+1}}{2\Delta z} + \frac{c_{i,j,k+1}^{t} - c_{i,j,k-1}^{t}}{2\Delta z} \right) \tag{15}$$

$$\frac{\partial^2 c}{\partial x^2} \to \frac{1}{2}\left( \begin{array}{l} \dfrac{c_{i+1,j,k}^{t+1} - 2c_{i,j,k}^{t+1} + c_{i-1,j,k}^{t+1}}{\Delta x^2} \\ + \dfrac{c_{i+1,j,k}^{t} - 2c_{i,j,k}^{t} + c_{i-1,j,k}^{t}}{\Delta x^2} \end{array} \right) \tag{16}$$

$$\frac{\partial^2 c}{\partial y^2} \to \frac{1}{2}\left( \begin{array}{l} \dfrac{c_{i,j+1,k}^{t+1} - 2c_{i,j,k}^{t+1} + c_{i,j-1,k}^{t+1}}{\Delta y^2} + \\ \dfrac{c_{i,j+1,k}^{t} - 2c_{i,j,k}^{t} + c_{i,j-1,k}^{t}}{\Delta y^2} \end{array} \right) \tag{17}$$

$$\frac{\partial^2 c}{\partial z^2} \to \frac{1}{2}\left( \begin{array}{l} \dfrac{c_{i,j,k+1}^{t+1} - 2c_{i,j,k}^{t+1} + c_{i,j,k-1}^{t+1}}{\Delta z^2} + \\ \dfrac{c_{i,j,k+1}^{t} - 2c_{i,j,k}^{t} + c_{i,j,k-1}^{t}}{\Delta z^2} \end{array} \right) \tag{18}$$

$$\frac{\partial D}{\partial x} \to \frac{D_{i+1,j,k}}{2\Delta x} - \frac{D_{i-1,j,k}}{2\Delta x} \tag{19}$$

$$\frac{\partial D}{\partial y} \to \frac{D_{i,j+1,k}}{2\Delta y} - \frac{D_{i,j-1,k}}{2\Delta y} \tag{20}$$

$$\frac{\partial D}{\partial z} \to \frac{D_{i,j,k+1}}{2\Delta z} - \frac{D_{i,j,k-1}}{2\Delta z} \tag{21}$$

$$\rho c - G(t)c \to \frac{1}{2}\left( \begin{array}{l} \rho^{t+1} c_{i,j,k}^{t+1} - G^{t+1} c_{i,j,k}^{t+1} + \\ \rho^{t} c_{i,j,k}^{t} - G^{t} c_{i,j,k}^{t} \end{array} \right) \tag{22}$$

where $c_{i,j,k}^{t}$ stands for the finite-difference approximation of $c$ at the point $(x_i, y_j, z_k)$ at time $t$, $\Delta t$ denotes the time step size, and $\Delta x$, $\Delta y$, $\Delta z$ are the space step sizes along each axis of the gridding scheme for the discretization in space. In the case that $\rho, G$ are time independent and $\Delta x = \Delta y = \Delta z = h$, the following equation is obtained:

$$\begin{aligned} & - \left[ \begin{array}{l} \left( \lambda_{i,j,k} + \dfrac{\lambda_{i+1,j,k} - \lambda_{i-1,j,k}}{4} \right) c_{i+1,j,k}^{t+1} + \\ \left( \lambda_{i,j,k} - \dfrac{\lambda_{i+1,j,k} - \lambda_{i-1,j,k}}{4} \right) c_{i-1,j,k}^{t+1} \end{array} \right] \\ & - \left[ \begin{array}{l} \left( \lambda_{i,j,k} + \dfrac{\lambda_{i,j+1,k} - \lambda_{i,j-1,k}}{4} \right) c_{i,j+1,k}^{t+1} + \\ \left( \lambda_{i,j,k} - \dfrac{\lambda_{i,j+1,k} - \lambda_{i,j-1,k}}{4} \right) c_{i,j-1,k}^{t+1} \end{array} \right] \\ & - \left[ \begin{array}{l} \left( \lambda_{i,j,k} + \dfrac{\lambda_{i,j,k+1} - \lambda_{i,j,k-1}}{4} \right) c_{i,j,k+1}^{t+1} + \\ \left( \lambda_{i,j,k} - \dfrac{\lambda_{i,j,k+1} - \lambda_{i,j,k-1}}{4} \right) c_{i,j,k-1}^{t+1} \end{array} \right] \\ & + \left[ 1 + 6\lambda_{i,j,k} - \frac{\Delta t}{2}(\rho - G) \right] c_{i,j,k}^{t+1} \end{aligned} \tag{23}$$

$$\begin{aligned} = & + \left( \lambda_{i,j,k} + \frac{\lambda_{i+1,j,k} - \lambda_{i-1,j,k}}{4} \right) c_{i+1,j,k}^{t} \\ & + \left( \lambda_{i,j,k} - \frac{\lambda_{i+1,j,k} - \lambda_{i-1,j,k}}{4} \right) c_{i-1,j,k}^{t} \\ & + \left( \lambda_{i,j,k} + \frac{\lambda_{i,j+1,k} - \lambda_{i,j-1,k}}{4} \right) c_{i,j+1,k}^{t} \\ & + \left( \lambda_{i,j,k} - \frac{\lambda_{i,j+1,k} - \lambda_{i,j-1,k}}{4} \right) c_{i,j-1,k}^{t} \\ & + \left( \lambda_{i,j,k} + \frac{\lambda_{i,j,k+1} - \lambda_{i,j,k-1}}{4} \right) c_{i,j,k+1}^{t} \\ & + \left( \lambda_{i,j,k} - \frac{\lambda_{i,j,k+1} - \lambda_{i,j,k-1}}{4} \right) c_{i,j,k-1}^{t} \\ & + \left[ 1 - 6\lambda_{i,j,k} + \frac{\Delta t}{2}(\rho - G) \right] c_{i,j,k}^{t} \end{aligned}$$

where

$$\lambda_{i,j,k} = \frac{D_{i,j,k}\Delta t}{\left[ 2(h)^2 \right]} \tag{24}$$

To apply the boundary condition in the numerical sense at any given grid point $(x_i, y_j, z_k)$, "fictitious nodes" are introduced. Their number is equal to the number of the adjacent nodes belonging to the boundary material (eg, skull). Evaluating the boundary condition at the point $(x_i, y_j, z_k)$ in the positive $y$ direction yields the following equation:

$$\left. \frac{\partial c}{\partial y} \right|_{(x_i, y_j, z_k)} = 0 \Rightarrow c_{i,j-1,k} = c_{F_{i,j+1,k}} \tag{25}$$

where $F_{i,j,k}$ stands for a fictitious node.

In theory, each node of the computational mesh may have a number of combinations of neighbors belonging to the adiabatic boundary material which is calculated by all combinations of $x+$ and $x-$, $y+$ and $y-$, and $z+$ and $z-$ directions as $\binom{6}{1} + \binom{6}{2} + \binom{6}{3} + \binom{6}{4} + \binom{6}{5} + \binom{6}{6} = 63$. However, to end up with a manageable but still realistic number of combinations, those combinations for which the node lies next to the boundary material in both the $x+$ and $x-$ directions and/or in both the $y+$ and $y-$ directions and/or in both the $z+$ and $z-$ directions have not been taken into account. These extreme cases do not appear to be of practical applicability in the problem addressed because the inner skull surface appears to be fairly smooth in the spatial discretization scale considered. Therefore, the total number of different node neighborhood topologies—referring to the existence of adjacent nodes in the boundary material—that have been considered is 26. For the boundary point in the negative $z$ and positive $y$ directions, equation (23) can be written in the following form:

$$
\begin{aligned}
&\left[1+6\lambda_{i,j,k}-\frac{\Delta t}{2}\left(\rho-G\right)\right]c_{i,j,k}^{t+1}\\
&-\left(\lambda_{i,j,k}+\frac{\lambda_{i+1,j,k}-\lambda_{i-1,j,k}}{4}\right)c_{i+1,j,k}^{t+1}\\
&-\left(\lambda_{i,j,k}-\frac{\lambda_{i+1,j,k}-\lambda_{i-1,j,k}}{4}\right)c_{i-1,j,k}^{t+1}\\
&-2\lambda_{i,j,k}c_{i,j-1,k}^{t+1}\\
&-2\lambda_{i,j,k}c_{i,j,k+1}^{t+1}\\
&=\left[1-6\lambda_{i,j,k}+\frac{\Delta t}{2}\left(\rho-G\right)\right]c_{i,j,k}^{t}+2\lambda_{i,j,k}c_{i-1,j,k}^{t}\\
&+\left(\lambda_{i,j,k}+\frac{\lambda_{i+1,j,k}-\lambda_{i-1,j,k}}{4}\right)c_{i+1,j,k}^{t}\\
&+\left(\lambda_{i,j,k}-\frac{\lambda_{i+1,j,k}-\lambda_{i-1,j,k}}{4}\right)c_{i-1,j,k}^{t}\\
&+2\lambda_{i,j,k}c_{i,j-1,k}^{t}\\
&+2\lambda_{i,j,k}c_{i,j,k+1}^{t}
\end{aligned}
\tag{26}
$$

The system of equations resulting from equation (1) through the previous processing can be equivalently written in the following form:

$$\vec{\vec{A}}\,\vec{x}=\vec{b} \tag{27}$$

where $\vec{x}$ represents a vector containing an approximation of the concentration $c$ at the mesh nodes at time $t$. It should be noted that the symbol $\vec{x}$ in equation (27) does not represent the generic spatial vector as used, eg, in equation (1). It should be pointed out that the coefficient matrix $\vec{\vec{A}}$ in equation (27) is a nonsymmetric and nonpositive definite sparse matrix. A vast array of variants of the conjugate gradient method have been developed for general linear systems, including the generalized minimal residual method, the quasiminimal residual method, the squared conjugate gradient method, the BiCG biconjugate gradient method (BiCG) method, and the stabilized biconjugate gradient (BiGSTAB) method. The technique selected for the solution of equation (27) is the BiCG method which replaces the orthogonal sequence of residuals by 2 mutually orthogonal sequences.[42]

It is worth noting that an alternative approach to the numerical solution of the main equation (1) could be the omission of the application of the chain rule in the continuous context and the direct discretization of the same equation.[43] In a study by LeVeque,[43] it is noted that the matrix corresponding to $\vec{\vec{A}}$ in equation (27) has certain advantages, such as being symmetric. Therefore, it seems worth exploring this alternative approach. The latter will be addressed in future work.

## Generic Error Estimation Checks

Several quantitative checks have been performed to estimate the accuracy of the numerical approaches implemented for solving equation (1). It is noted that pure diffusion, ie, zero tumor cell birth and death rates, has been considered in all computational scenarios performed in the rest of this particular section. Alternatively, the reaction-diffusion aspects of the model could be validated through the use of traveling wave solutions of the Fisher-Kolmogorov equation. The latter will be part of future work. Exact traveling wave solutions in the 1-dimensional reaction-diffusion models of glioblastoma growth are introduced in a study by Harko and Mak.[44] Publication by Gerlee and Nelander[45] analyzes the behavior of glioblastoma growth focusing on the properties of traveling wave solutions whose wave speed depends on the rates of phenotypic switching.

### *Comparison of the numerical with the analytical solution for a particular case*

To partly validate the numerical approach of the model, a comparison between the numerical and analytical solutions for a simplified homogeneous initial value problem has been conducted. The analytical solution for the problem described below is available in a study by Khan and Liu.[46] Thus, if $R=\Omega$ is the domain and $\partial R=\partial\Omega$ is the boundary, then the initial concentration $c$ at any spatial point $\vec{x}$ for the special case under consideration is supposed to be as follows:

$$
\underset{\vec{x}\,\varepsilon\,\Omega,\ \text{initial condition}}{c\left(\vec{x},0\right)=\exp\left[-\left(\frac{(x-x_0)^2}{2\sigma_0^2}+\frac{(y-y_0)^2}{2\sigma_0^2}+\frac{(z-z_0)^2}{2\sigma_0^2}\right)\right]},
\tag{28}
$$

where $\sigma_0$ is the standard deviation of the Gaussian function. For a domain without boundaries, the analytical solution of Gaussian distribution in 3 dimensions for pure diffusion is as follows:

$$
c\left(x,y,z,t\right)=\frac{\sigma_0^3}{\sigma^3}\exp\left(-\frac{(x-x_0)^2}{2\sigma^2}-\frac{(y-y_0)^2}{2\sigma^2}-\frac{(z-z_0)^2}{2\sigma^2}\right) \tag{29}
$$

$$
\sigma^2=\sigma_0^2+2Dt \tag{30}
$$

For $\sigma_0=3h$ and $t=n\Delta t$, where $h$ is the nodal spacing, $\Delta t$ is the time step, and $n$ is a counter for the time step, $\vec{x}=(x,y,z)$ stands for the spatial coordinates of the node, $(x_0,y_0,z_0)$ is the center of the cubic grid, $D$ stands for the diffusion coefficient, $c(\vec{x},t)$ denotes the concentration at the time point $t$ and at the spatial point $\vec{x}$, and $\lambda=D\Delta t/(2h^2)$. For the comparison of the analytical solution with the numerical solution, the size of the computational domain has been supposed to be large enough so that the application of the boundary conditions will not significantly affect the computations. Simulations have been performed for $\Delta t=0.5\,\text{day}$, $h=0.1\,\text{cm}$, and $D=0.0065\,\text{cm}^2/\text{d}$. The cancer cell concentration on the central axis of the discretizing mesh has been sampled at various time points, and the results of the comparison with the analytical solution are depicted in Figure 2. Obviously, there is

excellent agreement between the numerical and the analytical predictions.

### *Convergence and stability*

This section deals with an investigation of the stability and the convergence characteristics of the Crank-Nicolson method that has been used for the numerical solution of the GBM tumor growth and invasion model. For the initial value problem described in section "Comparison of the numerical with the analytic solution for a particular case," the cell density distribution in space and time has been calculated using the same value for the diffusion coefficient $D$ in gray matter, white matter, and CSF, which is equal to $0.0065\,\text{cm}^2/\text{d}$. The simulations have been executed for different values of the time step $\Delta t$ and the spatial step $h$, and the size of the computational domain has been assumed to be large enough so that the application of the boundary conditions will not significantly affect the computations. At the end of each simulation, the mean percentage error of the relative percentage error $e$ has been calculated. The relative percentage error is calculated by comparing the predicted values of $c$ generated by the model, with $c_{approx}$, ie, the ones obtained with the analytical solution. The relative error has been computed according to the following formula:

$$\text{Relative error} = \left|1 - \frac{c_{approx}}{c}\right| \tag{31}$$

Figure 3A summarizes the mean percentage error in the approximate solution at $t = 100\,\text{days}$ for different values of $h$ and fixed time step of $\Delta t = 0.5\,\text{days}$. Figure 3B presents the error of the approximate solution at $t = 100\,\text{days}$ for different values of $\Delta t$, with $h$ fixed at $0.1\,\text{cm}$. The total simulated time has been assumed to be 100 days. It is noted that the analytical solution does not take into account the boundaries, and consequently, a slight cell loss is expected to be observable after several days. Second-order accuracy of the method in both space and time has been achieved.

According to Figure 3, after 100 simulated days, the discrepancy between the numerical and analytical results is less than 1% for a temporal discretization unit equal to $1\,\text{day}$ and about 0.65% for a space discretization of $0.1\,\text{cm}$. For the case of $h = 0.75\,\text{cm}$, the mean percentage error reaches the value of 11%, which is reasonable because the spatial discretization of the domain that includes the tumor is too sparse. In the rest of the article and for the simulations performed, the values 0.5 day and 0.1 cm have been used for the time and space discretizations, respectively, so that reasonable levels of precision and accuracy can be achieved.

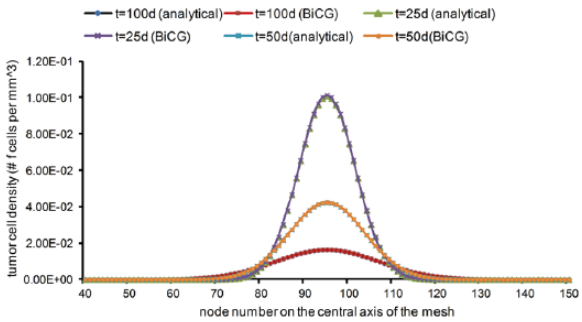


**Figure 2.** Comparison between the numerical solution (using the biconjugate gradient [BiCG] method) and the analytical one for the pure diffusion scenario. The concentration on the central axis of the discretizing mesh has been sampled at several time points ($t = 25\,\text{days}$, $t = 50\,\text{days}$, and $t = 100\,\text{days}$). The results have been obtained for the following parameter values: $\Delta t = 0.5\,\text{day}$, $h = 0.1\,\text{cm}$, $D = 0.0065\,\text{cm}^2/\text{d}$. Clearly, the numerical results are in excellent agreement with the analytical solution.

### *Linearity checks*

An initial ideal spherical tumor of diameter equal to 4 cm has been assumed inside a mesh of $101\,\text{mm} \times 101\,\text{mm} \times 101\,\text{mm}$. The initial cell concentration is assumed $10^6\,\text{cells/mm}^3$ inside

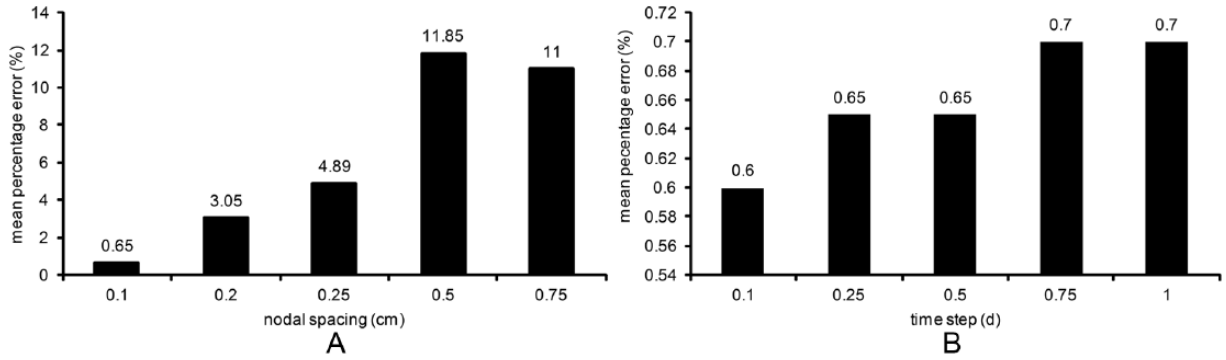


**Figure 3.** Error analysis of the model. The simulated domain has been assumed sufficiently large such that the application of the boundary conditions does not practically affect the computations in the region of interest. The diffusion coefficient $D$ has been assigned the value of $0.0065\,\text{cm}^2/\text{d}$. (A) Mean percentage error for a range of values of nodal spacing $h$. For all calculations, a constant/fixed time step of $\Delta t = 0.5\,\text{day}$ has been used and the approximate solution has been obtained at $t = 100\,\text{days}$. (B) Mean percentage error for a range of values of time step $\Delta t$. For all calculations, a constant nodal spacing $h = 0.1\,\text{cm}$ has been used and the approximate solution has been obtained at $t = 100\,\text{days}$.

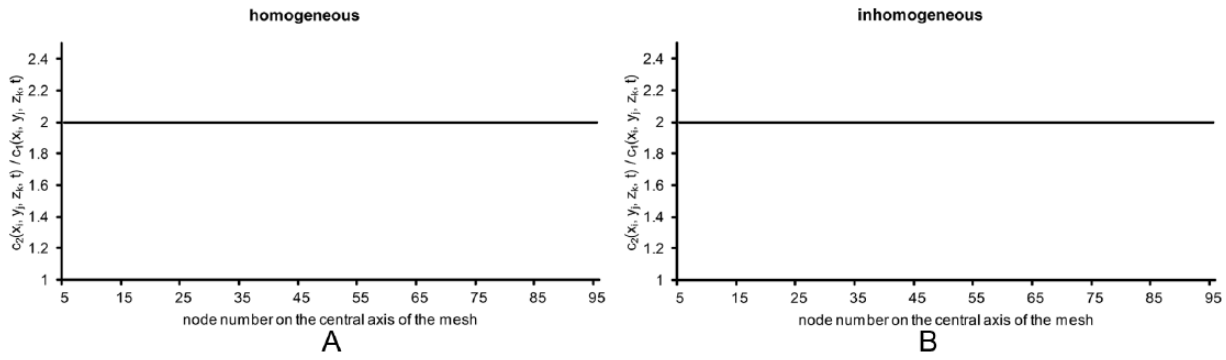


**Figure 4.** Checking linearity over a central axis of the discretizing mesh for (A) a homogeneous and (B) an inhomogeneous brain scenario. It is established that if the initial cancer cell concentration is doubled at all points of the discretizing mesh, the cancer cell concentration at any spatiotemporal point under consideration $(x_i, y_j, z_k, t)$ is doubled in relation to its value that corresponds to the reference initial cancer cell concentration.

the sphere and $0\,\text{cells/mm}^3$ outside the sphere. Two cases of pure diffusion (no sources, no sinks) have been considered: homogeneous and inhomogeneous. In the first case, the diffusion coefficient $D$ has been assigned the value $0.0065\,\text{cm}^2/\text{d}$. In the second case, the diffusion coefficient $D$ has been assigned the values $0.00051\,\text{cm}^2/\text{d}$ in white matter, $0.000102\,\text{cm}^2/\text{d}$ in gray matter, and $0.000001\,\text{cm}^2/\text{d}$ in CSF.

For the extreme hypothetical scenario of pure diffusion (absence of both sources and sinks), it has been ensured that if the initial cancer cell concentration is doubled at all points of the discretizing mesh, ie,

$$c_2\left(\vec{x},0\right) = 2c_1\left(\vec{x},0\right) \tag{32}$$

the cancer cell concentration at any spatiotemporal point $(\vec{x},t) = (x_i, y_j, z_k, t)$ is doubled regarding its value corresponding to the reference initial cancer cell concentration. Hence, the updated tumor cell concentration value at point $(x_i, y_j, z_k, t)$ is given by the following equation:

$$c_2\left(\vec{x},t\right) = 2c_1\left(\vec{x},t\right) \tag{33}$$

The concentration ratio $c_2(x_i, y_j, z_k, t) / c_1(x_i, y_j, z_k, t)$ is shown in Figure 4. Clearly, the ratio $c_2(x_i, y_j, z_k, t) / c_1(x_i, y_j, z_k, t)$ equals the ratio $c_2(x_i, y_j, z_k, 0) / c_1(x_i, y_j, z_k, 0)$. This observation serves as a validation of the purely diffusive linear part of the simulation code.

### *Mass conservation*

In the following nonbiologically relevant scenario where pure glioma cells diffuse within an isolated domain in which tumor cells can neither be generated nor disappear, mass conservation applies. The computational domain has been taken to be equal to $168\,\text{mm} \times 114\,\text{mm} \times 114\,\text{mm}$ so that it may roughly correspond to realistic dimensions of the human head but with a much simpler geometry. The diffusion coefficient $D$ has been assumed to be equal to $0.00051\,\text{cm}^2/\text{d}$ in white matter, $0.000102\,\text{cm}^2/\text{d}$ in gray matter, and $0.000001\,\text{cm}^2/\text{d}$ in CSF.

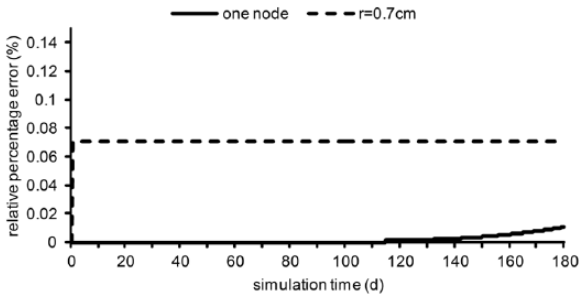


**Figure 5.** Relative percentage error of the total cancer cell population relating to its initial number for 2 cases in a closed and isolated system. In the first case, a fictitious growing glioblastoma tumor of spherical shape with a diameter equal to 1.4 cm has been virtually placed inside the cranial cavity. The initial cell concentration is assumed to be $10^6\,\text{cells/mm}^3$ inside the sphere and $0\,\text{cells/mm}^3$ outside the sphere. In the second case, 1 single node of dimension 1 mm³, with initial cell concentration equal to $10^6\,\text{cells/mm}^3$, has been assumed. Pure diffusion is considered for validation purposes only. The percentage error of the total number of tumor cells, which is principally the result of the replacement of the continuous expressions with their numerical counterpart, is less than 0.08% for a simulation time equal to 180 days.

Two cases have been considered. In the first one, an initial ideally spherical tumor of diameter equal to 1.4 cm has been located inside the discretizing mesh. The initial cell concentration is assumed to be $10^6\,\text{cells/mm}^3$ inside the sphere and $0\,\text{cells/mm}^3$ outside the sphere. In the second case, one single node of dimension 1 mm³, with initial cell concentration equal to $10^6\,\text{cells/mm}^3$, has been assumed. Simulation code runs have indicated that the total number of cancer cells inside the mesh remains practically stable with only minor deviations because of the accumulation of minimal numerical errors for a substantial time interval of 180 days. The relative percentage error of the total number of cancer cells in relation to the initial number of cancer cells is shown in Figure 5. It is pointed out that after 180 simulated days, the relative percentage error remains less than 0.08%.

## Numerical Experiments

Several *in silico* numerical experiments have been executed with the aim of checking the validity of the model presented. A

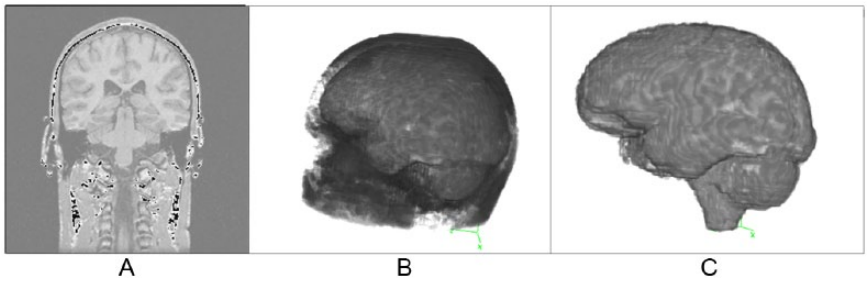


**Figure 6.** (A) Indicative (coronal) slice of the T1 head and brain image data set used in the *in silico* experiments of this article. The data set originates from the open-source software 3D Slicer freely available on the Internet. (B) Three-dimensional rendering of the data set used in the simulations. (C) Three-dimensional rendering of the same data set without the skull.

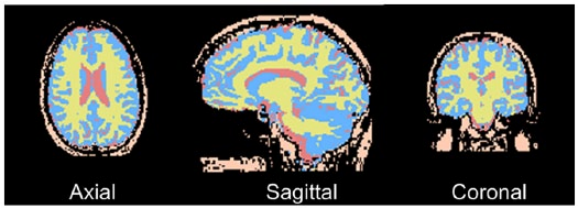


**Figure 7.** Indicative results of structure/region segmentation for a normal human head. Pink-colored regions represent background (air and skull), yellow-colored regions represent white matter, blue-colored regions represent gray matter, and red-colored regions represent cerebrospinal fluid.

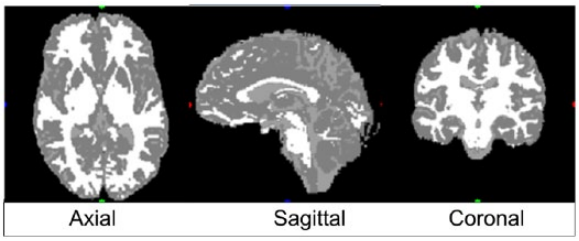


**Figure 8.** Indicative results of the segmentation in gray scale. Black color (red, green, blue [RGB] [0, 0, 0]) corresponds to anything outside the inner surface of the skull that defines the cranial cavity. This implies that black color can represent cranial bones, air, etc. White color (RGB [255, 255, 255]) corresponds to white matter, RGB (128, 128, 128) corresponds to gray matter, and RGB (160, 160, 160) corresponds to cerebrospinal fluid.

3D brain geometry has been considered. The data set used has been acquired from an open-source software (3D Slicer) freely available on the Internet.[47,48] The resource is an application for image analysis and automatic segmentation of brain structures from MRI data. A 3D rendering of the data set is depicted in Figure 6.

In the proposed model, the diffusion coefficient is a function of position $\vec{x}$, and subsequently, there has been a need to create virtual regions with different diffusivities. The structures/regions that have been segmented are white and gray matter, CSF, and skull (cranium). The 3D Slicer software has been used to superimpose the results of the segmentation on the original T1 images (Figure 7). Different colors correspond to different segmented structures. The acquired 3D Slicer tutorial data set consists of 124 slices of 1.5 mm thickness, with a voxel dimension of 0.9375 mm × 0.9375 mm × 1.5 mm and a resolution of 16 bits per pixel.

To accelerate the calculations without any loss of information, part of the image corresponding to air surrounding the skull has been cropped. Furthermore, because the discretization of the problem assumes a cubic lattice, a new cubic discretization of the data set–based anatomic region of interest has been performed. The new cubic voxel has a dimension of 1 mm × 1 mm × 1 mm. In addition, the resolution has been reduced to 8 bits per pixel using the ImageJ software.[49] Indicative sections of the reconstructed anatomic region of interest in gray scale are depicted in Figure 8. Because only the inner surface of the skull is used in the simulation executions, the 3D flat bone structure of the skull has been removed.

As a first approximation, and for cases where the primary glioblastoma tumor lies away from foramen magnum and other skull foramina, the latter are assumed to act as boundaries. This is justified by the very small expected number of GBM tumor cells lying close to them due to diffusion.

### *Model parameters*

A list of parameters serves as the input of the model. The typical values of the parameters that have been used for the production of the results have been carefully selected from pertinent literature so as to best reflect experimentally and clinically observed aspects of glioblastoma dynamics in both microscopic and macroscopic scales. Because GBM is a highly inhomogeneous tumor, the parameter values considered refer to a hypothetical "mean GBM cell."

Each value of the diffusion coefficient $D$ shown in Table 1 has been estimated as the average value of the migrating and the growing diffusion coefficient for each brain region.[5] The diffusion coefficient for corpus callosum and white matter has been considered the same. The latter has been estimated to be 5 times greater than for gray matter according to Swanson et al[50] because of the different motility of tumor cells in gray and white matter. According to Baldock et al,[51] malignant glioma cells can migrate up to 100-fold faster in white matter than in gray matter characterizing the extent of invisible subclinical disease. It is noted that the values of $D$ for both white

**Table 1.** Values of the diffusion coefficient *D* for the different structures of the human brain.

| STRUCTURE/REGION OF THE HUMAN BRAIN | DIFFUSION COEFFICIENT *D* ($CM^2/D$) |
|---|---|
| White matter | 0.00051 |
| Gray matter | 0.000102 |
| Cerebrospinal fluid | 0.000001 |
| Corpus callosum | 0.00051 |

and gray matter appearing in Table 1 are considerably lower than the corresponding values reported in a study by Swanson et al.[50] Using the computational approach presented and experimenting *in silico* could contribute to the optimal selection of diffusion coefficient values by comparing the predictions of the model with actual clinical data.

The abrupt and frequent changes of the value of $D$ between the different brain matters (gray and white) and CSF, as well as the unavoidable quantization/discretization errors created during the numerical solution of the problem, have led to certain negative values of the computed tumor cell concentration. It should be noted that the problem of handling negative concentrations which appear during the numerical solution of partial differential equations is still an open issue. Several approaches to alleviate this problem have been suggested (ie, Discussion Forum[52]). We have tried a number of them but without any significant and staying improvement, apparently due to the fact that the value of the diffusion coefficient *D* between 2 adjacent nodes, one of which lies within the CSF, changes sharply. Therefore, we have resorted to the simple solution proposed by John et al,[53] and the negative concentrations have just been cut off.

It is also noted that the percentage of the sum of the tumor cell concentration negative values per node per execution cycle (that have been cut off) over the total number of tumor cells corresponding to the same execution cycle, in the simulations of section "Numerical Experiments" and for a total simulation time equal to 180 days, varies between 0.00106% and 0.0022%. This means that the overall error due to the cutting off of negative values is negligible.

The net tumor growth rate $\rho$ refers to the resultant of tumor cell proliferation, loss, and death. Different combinations of $D$ and $\rho$ values can simulate multiple tumor grades. High $\rho$ and high $D$ refer to a high-grade tumor, (high $\rho$ and low $D$) or (low $\rho$ and high $D$) refer to an intermediate-grade tumor, and low $\rho$ and low $D$ refer to a low-grade tumor.[50] It has been suggested in a study by Swanson[37] that a typical value of $\rho$ is 0.012 units/d. It has also been reported in a study by Stein et al[54] that the maximum growth rate for glioma cells is 0.3 units/d. Because there appears to be a controversy regarding the most plausible values of the parameters $D$ and $\rho$, several combinations of the values mentioned above have been considered in this article. Glioblastoma diagnosis is practically possible after the tumor has reached a tomographically imageable size equivalent to a sphere with an average diameter of 3 cm.[55]

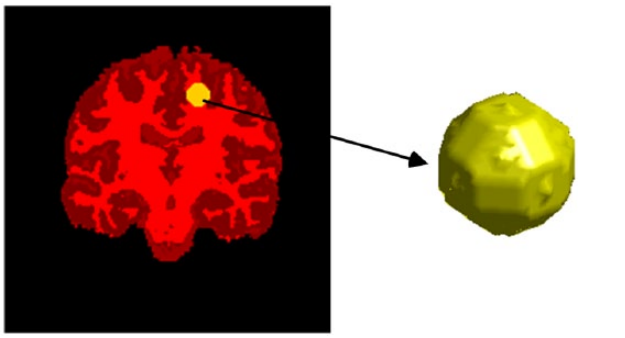

**Figure 9.** A virtual glioblastoma tumor of spherical shape with a diameter equal to 1.4 cm has been assumed inside the cranial cavity. For simplicity and clarity reasons, only the brain is shown. Before the start of the simulation, diffusion phenomena are not taken into account The concentration threshold for tumor visualization when the tumor has been virtually extracted from the brain (for improved visualization) has been taken equal to $1\,cell/mm^3$.

Following the completion of the data set image segmentation, cubic voxel resampling, and 3D reconstruction of the anatomic region of interest, we have proceeded to *in silico* experimentation. A hypothetical glioblastoma tumor of ideally spherical shape with a diameter equal to 1.4 cm has been located inside the cranial cavity (Figure 9). Such a relatively large initial spherical tumor has been assumed to accelerate the simulation execution process. To achieve a more refined simulation of the time course of glioblastoma, one could start the simulation by placing an initial tumor of a smaller diameter of about $1\,mm^3$ at the same position. In such a case, the computing requirements would obviously be considerably higher.

For the sake of simplicity, during the process of the *in silico* model validation, the cancer cell concentration within the initial tumor has been arbitrarily hypothesized uniform and equal to $10^6$ cells/$mm^3$. This concentration value is a realistic estimate for at least a small avascular glioma tumor of volume equal to $1\,mm^3$ according to the literature.[36] Regarding the parameters associated with the numerical methods used, the following values have been selected. The convergence tolerance for the BiCG method has been chosen to be equal to $10^{-6}$. The treatment loss rate has been assumed to be equal to 0 implying that no therapy is administered. Before the start of the simulation, diffusion phenomena are not taken into account. The longest simulated time considered has been 180 days.

## *Results*

First, to validate the pure diffusion component of the proposed model as well as the accuracy of the numerical implementation of the Neumann boundary conditions, both the net tumor growth rate $\rho$ and the treatment loss rate $G(t)$ have been assumed to be equal to 0. In such a scenario within a hypothetically closed

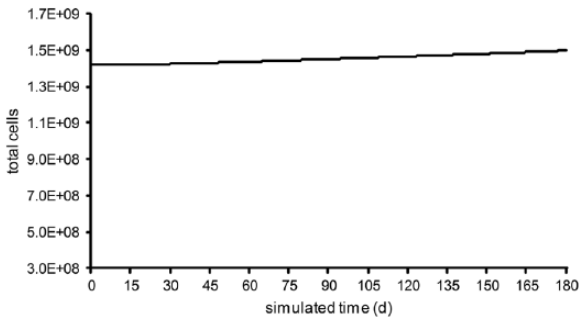


**Figure 10.** Time course of the total cancer cell population corresponding to the case of pure diffusion. The time step $\Delta t$ and the space step size $h$ have been assumed to be equal to $0.5\,\text{day}$ and $0.1\,\text{cm}$, respectively. At the start of the simulation, an initial fictitious growing glioblastoma tumor of spherical shape with a diameter equal to 1.4 cm and uniform tumor cell concentration equal to $10^6\,\text{cells/mm}^3$ has been virtually placed inside the cranial cavity. The total number of cells remains practically unchanged with only slight fluctuations across computer simulations. This implies good accuracy of the diffusive component of the model.

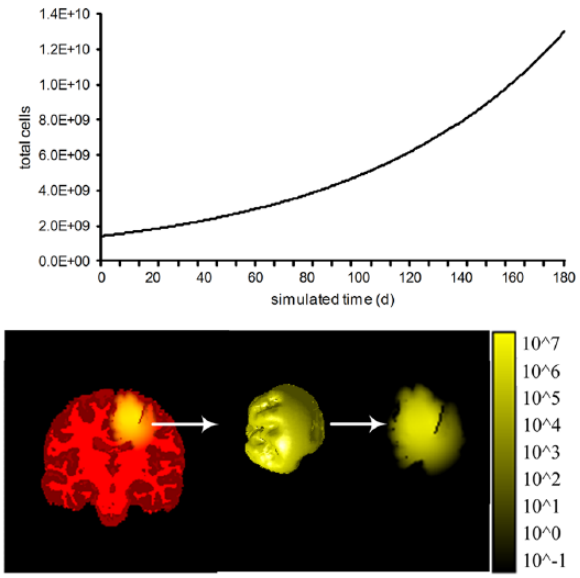


**Figure 11.** Predicted number of total tumor cells as a function of time and spatial distribution of the tumor material after a simulated time interval of 180 days ($\rho = 0.012\,/\,\text{d}$, the values assigned to the rest of the parameters are reported in the main text). For simplicity and clarity reasons, only the brain is shown. The size of each voxel is $1\,\text{mm} \times 1\,\text{mm} \times 1\,\text{mm}$. The initial condition of Figure 9 is considered. The threshold for tumor visualization when the tumor has been virtually extracted from the brain has been taken equal to 1 cell/mm³. The color bar on the right-hand side refers to the tumor cell concentration $c$ (cells per mm³). Denoting the color intensity–level function of $c$ by $I(c)$, the corresponding equation is $I = k \log_{10} c$, where the constant $k = 255 / \log_{10} c_{\max}$ and $c_{\max}$ stands for the maximum value of tumor cell population which is observed during the experiment. It is assumed that $I = 0$ for cell concentration less than $1\,\text{cell/mm}^3$.

cranial cavity, tumor cell mass conservation must apply. It should be stressed that this biologically impertinent scenario has been considered exclusively for the needs of partial mathematical validation of the analysis presented. Numerical code runs have shown that the total number of cancer cells inside the discretizing mesh remains practically stable with only minor deviations due to the piling up of minimal numerical errors for a substantial time interval (Figure 10). This is an important indication of the correctness of the purely diffusive part of the model.

In a second numerical experiment, the value of the net tumor growth rate has been taken to be equal to $\rho = 0.012\,/\,\text{d}$. The predicted number of total tumor cells as a function of time, as well as the spatial distribution of the tumor material after a simulated time interval of 180 days, is depicted in Figure 11. The concentration threshold for tumor visualization when the tumor has been virtually extracted from the brain for improved visualization purposes has been taken to be equal to 1 cell/mm³.

A typical coronal slice of the virtual tumor at different time points is depicted in Figure 12.

The simulated tumor cell density (cells per mm³) along the $x$ axis (the horizontal axis of the coronal plane) passing through the center of the initial tumor for the time points of 60, 120, and 180 days is depicted in Figure 13.

Due to the infiltrating nature of malignant gliomas, diagnostic tools such as computerized tomography (CT) and MRI cannot detect the outer tumor border with accuracy. According to Swanson et al,[55] the threshold of tumor detection for the enhanced CT corresponds to $8000\,\text{tumor cells/mm}^3$. For the simulations performed in this article, the above-mentioned threshold value has been assumed as a first approximation for T1 gadolinium–enhanced MRI. Figure 14 provides a visualization of the growth of a virtual glioblastoma tumor on the simulation starting day, the 60th day, the 120th day, and the 180th day. It is noted that the strongly pseudocolored part of the tumor is delimited by the CSF which lies between the gray matter and the skull. Diffusion within the CSF is small according to Table 1.

To estimate the accuracy of the approach, the error of the aforementioned example referring *only* to the predicted number of cancer cells and *not* their spatial distribution has been calculated. An estimate of the error has been produced by comparing the total number of cancer cells as predicted by the proposed model with the corresponding prediction of exponential growth. The latter is the simplest proliferation law and was proposed by Malthus in 1798. The Malthus law in our case provides the cancer cell population $P(t)$ within a hypothetically "closed" skull cavity at any time $t$ as a function of the initial cancer cell population $P(0)$ and the constant growth rate $k$, which in the tumor growth framework addressed depends on the intrinsic net tumor growth rate (aggressiveness of the tumor), ie,

$$P(t) = P(0)e^{kt} \tag{34}$$

The computational error of the numerical method is obtained using equation (31) where $c$ is the concentration calculated using exponential growth and $c_{approx}$ is the numerically

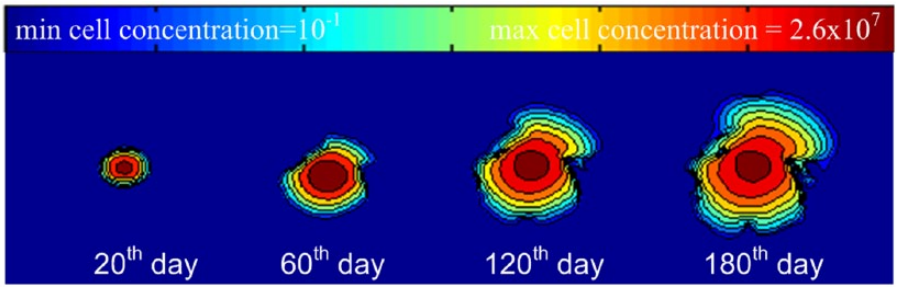


**Figure 12.** Typical contour plot (coronal section) of the tumor cell density (concentration) corresponding to the initial virtual glioblastoma multiforme tumor of Figure 9 of radius equal to 0.7 cm at different time points of the simulated tumor growth (20, 60, 120, and 180 days). Zero and maximum cell concentration in this figure correspond to dark blue and dark red, respectively. The color bar scale is logarithmic and corresponds to the tumor cell concentration (cells per mm$^3$). The value of the net tumor growth rate is 0.012 units/d. The threshold of tumor cell detection and visualization has been taken to be equal to $1\,\text{cell/mm}^3$.

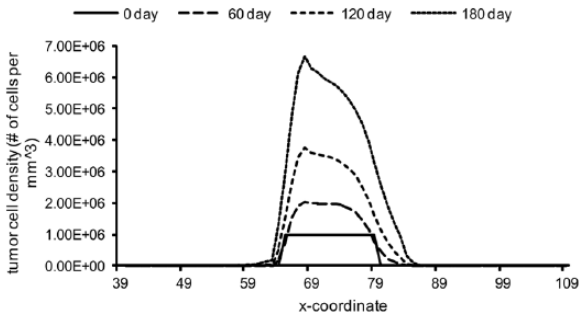


**Figure 13.** Tumor cell density (number of tumor cells per mm$^3$) along the *x* axis (the horizontal axis of the coronal plane) passing through the center of the initial tumor for different simulated time points (60, 120, and 180 days) and a spatially dependent diffusion coefficient. The initial condition of Figure 9 is assumed.

calculated concentration. Figure 15 shows the error variation for different values of $dt$. For all $\Delta t$ values, the error is essentially the same. It should be noted that the complexity of the brain structures bounded by the skull is very high. This unavoidably leads to spatial discretization errors. The latter can explain an error of approximately 5% after the relatively large time interval of 180 simulated days.

The simulated tumor cell density for different values of net tumor growth rate (including 2 values reported in literature as well as 2 hypothetical values) is depicted in Figure 16. Panel (A) shows the total number of tumor cells obtained 180 days after the start of the simulation. Panel (B) shows the density of tumor cells (number of tumor cells per mm$^3$) along the *x* axis (the horizontal axis of the coronal plane) passing through the center of the initial tumor. The diffusion coefficient values adopted for the various structures/regions of the brain are shown in Table 1.

According to Swanson et al,[50] the following estimates of typical glioblastoma doubling time, $T_d$, and growth rate have been reported in the literature:

1. Doubling times for gliomas range from 1 week to 12 months covering the range of high- to low-grade gliomas.[56]
2. For glioma with growth rate equal to 0.012/d, the doubling time is expected to be equal to 2 months.

For the assessment of clinical validity, 2 clinically measured values of doubling time have been used. Therefore, no claims for a statistical validation of the model can be made in this article. However, the article does outline a realistic procedure for a possible partial clinical validation of the model in the future. For the calculation of the doubling time, the latter being a quantity of critical importance in the course of the disease, 2 cases of combining values of parameters $D, \rho$ have been considered, as shown in Table 2.

It appears that the value combinations for $D, \rho$ appearing in Table 2 are quite realistic choices based on the literature. The calculated doubling time as a function of simulated time is depicted in Figure 17. It is more usual to find that $T_d$ increases progressively as the tumor becomes bigger.[36] It can be readily noticed that in all simulated cases, the calculated values of doubling time are in agreement with those reported in the literature for high-grade gliomas.

A typical value for the doubling time, for $\rho = 0.012$/day, is 2 months.[50] In the first case, this is observed on the 33th simulated day. It is noted that the doubling time which spans between the initial simulated time point and the time point at which the tumor has doubled is assumed to correspond to the initial simulated time point. The graphs of Figure 17 constitute parts of typical Gompertzian growth curves. Gompertzian growth is well known to be able to model macroscopic tumor growth in a phenomenologic context. This can explain the increasing doubling time as a function of time.

Finally, for the scenario described above, a comparison of the results for the homogeneous and inhomogeneous cases has been undertaken. For the homogeneous case, the diffusion coefficient $D_{wa}$ has been calculated as the weighted average value of $D$ taking into account the volume for which each diffusion coefficient value holds true and has been found to be equal to $0.00038\,\text{cm}^2/\text{day}$. In symbols,

$$D_{wa} = \frac{D_w \cdot N_w + D_g \cdot N_g + D_{CSF} \cdot N_{CSF}}{N_w + N_g + N_{CSF}} \qquad (35)$$

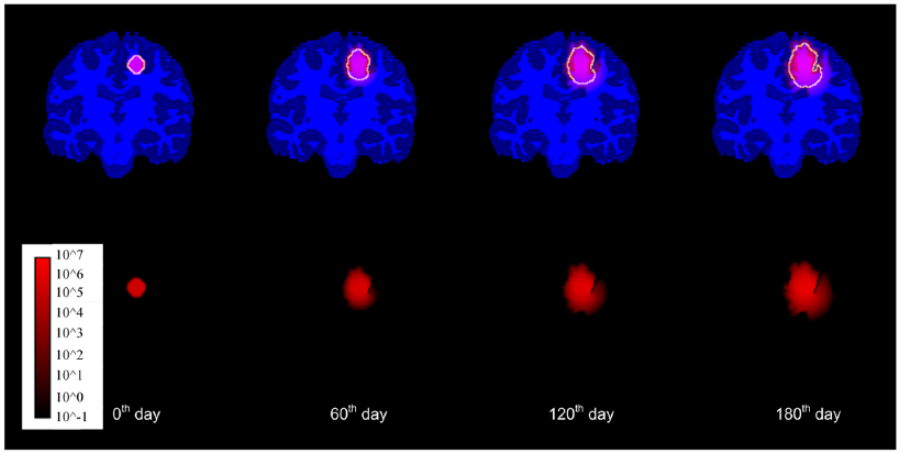


**Figure 14.** Visualization of a virtual glioblastoma tumor growth in vivo on a coronal slice at various time points. For simplicity and clarity reasons, only the brain is shown. The initial condition of Figure 9 is considered. Denoting the color intensity–level logarithmic function of $c$ by $I(c)$, the corresponding equation is $I = k\log_{10} c$, where the constant $k = 255/\log_{10} c_{\max}$ and $c_{\max}$ stands for the maximum value of tumor cell population which is observed during the experiment. The threshold for tumor visualization has been taken to be equal to $1\,\text{cell/mm}^3$. The bright contour loop generated on the upper raw corresponds to the tomographically detectable tumor boundary at a detection level of $8000\,\text{cells/mm}^3$.

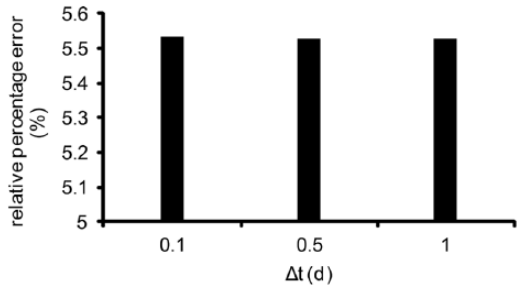


**Figure 15.** Error variation for different values of $\Delta t$ at 180 simulated days after the start of the simulation by comparing the results from the proposed model with those obtained through the use of exponential growth (golden standard). The initial condition of Figure 9 is assumed. The space step size has been taken equal to 0.1 cm.

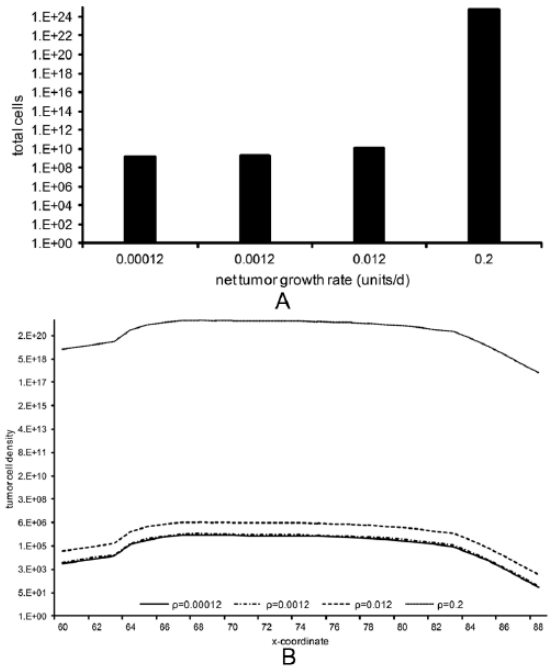


**Figure 16.** Effect of varying the net tumor growth rate on the growing and diffusive behavior of glioblastoma multiforme. The initial condition of Figure 9 is assumed. The values 0.012 and 0.2 units/d have been reported in the literature. Two additional hypothetical values have been considered. In panel (A), the total cell population at the 180th day of simulation is depicted. It is noted that the value of the total cell population for $\rho = 0.2$ units/d on the 180th simulated day may have only theoretical meaning because it cannot be physically accommodated within the cranial cavity. The patient must have already died in such a case. Panel (B) shows the density of tumor cells (number of tumor cells per mm3) along the $x$ axis passing through the center of the initial tumor.

where $N_w$ is the number of (discretizing mesh) nodes which belongs to the white matter region, $N_g$ is the number of nodes which belongs to the gray matter region, and $N_{CSF}$ is the number of nodes which belongs to the CSF region of the CT imageable part of the simulated tumor on the 180th day using the inhomogeneous model.

The above weighted average has also been calculated by taking into account the part of the tumor for which the cell concentration is greater than $8000\,\text{cells/mm}^3$. In that case, its value has been found to be equal to $0.00034\,\text{cm}^2/\text{d}$. The doubling time for the homogeneous and inhomogeneous cases and for net tumor growth rate equal to 0.012 units/d is depicted in Figure 18. Three cases of combinations of $D$ values have been considered, as shown in Table 3.

The *in silico* simulation results for the scenarios considered (Figure 18) indicate that using the homogeneous normal brain-based model may produce an error of up to 10% for the first 25 simulated days in relation to the predictions of the inhomogeneous model. This observation suggests that even by using a homogeneous brain-based model in conjunction with an adequately weighted average value of its diffusion coefficient, a rough but nonetheless informative estimate of the expected

**Table 2.** Combinations of values for the parameters $D, \rho$.

| CASE | DIFFUSION COEFFICIENT ($CM^2/D$) | NET TUMOR GROWTH RATE (UNITS/D) |
|---|---|---|
| 1 | $D_w = 0.00051, D_g = 0.000102, D_{CSF} = 0.000001$ | 0.012 |
| 2 | $D_w = 0.00051, D_g = 0.000102, D_{CSF} = 0.000001$ | 0.2 |

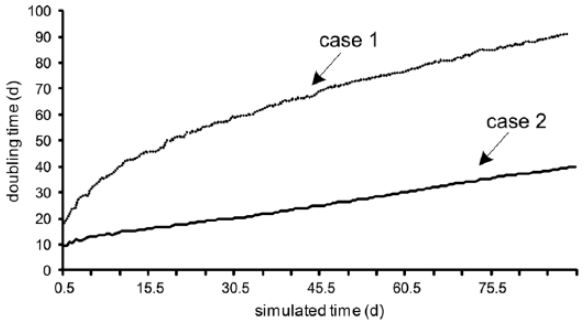


**Figure 17.** Doubling time as a function of simulated time. The initial condition of Figure 9 is assumed. In case 1, the value of net tumor growth rate has been assumed to be equal to 0.012 units/d. In case 2, the value of the same parameter has been assumed to be equal to 0.2 units/d. In both cases, the diffusion coefficient values adopted for the various regions of the brain are as follows: $0.00051\,cm^2/d$ for the diffusion coefficient in white matter, $0.000102\,cm^2/d$ for the diffusion coefficient in gray matter, and $0.000001\,cm^2/d$ for the diffusion coefficient in cerebrospinal fluid.

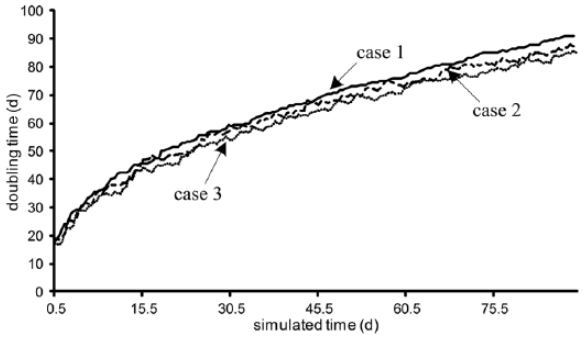


**Figure 18.** Doubling time as a function of simulated time for a homogeneous and an inhomogeneous brain model and for net tumor growth rate equals $0.012$ units/d. The initial condition of Figure 9 is assumed. Three cases of combinations of $D$ values have been considered. The first case corresponds to an inhomogeneous model. The values used for $D$ in white matter, gray matter, and cerebrospinal fluid are $0.00051, 0.000102$, and $0.000001\,cm^2/d$, respectively. The second and third cases correspond to a homogeneous model. The values for the diffusion coefficient are $0.00034$ and $0.00038\,cm^2/d$, respectively.

tumor doubling time can be achieved. It is pointed out that the values of the diffusion coefficients and the cell birth and death rates of the model can undergo substantial refinement and personalization through the exploitation of histologic and molecular data of the patient. This kind of work undertaken by our research group is in progress.

A visualization of the virtual glioblastoma tumor growth is depicted in Figure 19.

For further validation of the model presented, additional scenarios regarding the initial virtual glioblastoma tumor condition have been considered. The results of the simulation are presented in Figure 20. It is noted that on the first, third, and fourth columns of Figure 20, the initial tumor has been assumed to be the same (ie, a hypothetical spherical tumor with cell density equal to $10^6$ tumor cells/$mm^3$). The rest of the parameter values adopted in all cases of Figure 20 ($D$, $\rho$, $h$, $\Delta t$) are the same. However, the spatial GBM tumor cell distribution as time passes differs considerably among cases 1, 3, and 4. This can be readily explained by taking into account the differing nearest inner skull surface curvature in conjunction with the differing detailed local geometry of the regions occupied by white matter, gray matter, and CSF.

Execution of the computer code for 6 simulated months and a discretizing mesh of $178 \times 178 \times 178$ nodes, each one of dimensions $1\,mm \times 1\,mm \times 1\,mm$ on a 32-bit Windows Vista Platform machine (4 GB RAM and processor Intel Core 2 Duo CPU P8600@2.4 GHz), takes about 10 minutes. Use of more processors is expected to improve this time.

## Discussion

The major highlight of the article is the numerical handling of the Neumann boundary conditions imposed by the cranium on an inhomogeneous diffusion-reaction model of glioma growth and invasion in 3 dimensions. If the adiabatic Neumann boundary conditions are not properly applied to GBM invasion modeled by reaction-diffusion, it is almost certain that there will be artificial loss of tumor cells. This is, eg, the case when the much simpler to apply Dirichlet boundary conditions are adopted as a crude (and admittedly much less demanding) substitute for the correct Neumann conditions. An application of Dirichlet boundary conditions may lead to a lower predicted probability for tumor regrowth following treatment (ie, chemotherapy, radiotherapy, and combined therapy). Such a scenario may subsequently lead to more optimistic expectations regarding tumor growth or regrowth than what happens in reality. Exploratory *in silico* experimentation by the authors has supported the above remarks. Therefore, we think that it is important not to bypass an explicit and correct application of the Neumann boundary conditions to the problem under consideration.

From a different perspective, GBM growth, invasion, and response to treatment are clearly multiscale phenomena. In this context, an in-depth theoretical analysis of tumor dynamics should not be constrained to a small number of biocomplexity

**Table 3.** Combinations of *D* values considered.

| CASE | DIFFUSION COEFFICIENT ($CM^2/D$) | APPROACH |
|---|---|---|
| 1 | $D_w = 0.00051$, $D_g = 0.000102$, $D_{CSF} = 0.000001$ | Inhomogeneous |
| 2 | $D_w = D_g = D_{CSF} = 0.00034$ | Homogeneous |
| 3 | $D_w = D_g = D_{CSF} = 0.00038$ | Homogeneous |

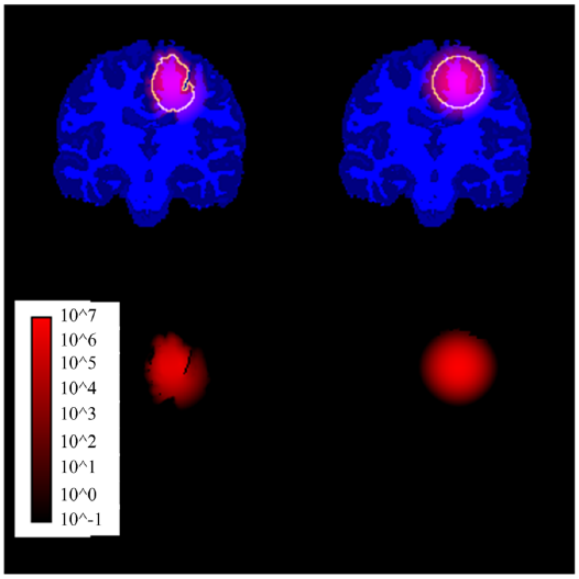


**Figure 19.** Coronal view of simulated magnetic resonance images of the growth of a fictitious glioblastoma multiforme tumor in vivo generated on the 180th simulated day for the inhomogeneous (left panel) and homogeneous cases (right panel) at a detection level of $1\,\text{cell/mm}^3$. For simplicity and clarity reasons, only the brain is shown. The initial condition of Figure 9 is assumed. The color intensity level is a logarithmic function of *c*. The outer bright contours of the slices correspond to the tomographically detectable tumor boundary at a detection level of $8000\,\text{cells/mm}^3$.

levels. Because, however, the model presented focuses on the spatiotemporal characteristics of glioblastoma invasion, a cellular-, tissue-, and organ-scale (or level) approach appears to be a good basis for modeling the involved biomechanisms. The effects of subcellular molecular mechanisms could also be summarized as perturbators of the population-based average values of the parameters ρ, *D*, and $G(t)$. Because the exact microscopic structure of neovasculature is unknown, considering a mean neovasculature density throughout the brain is a plausible mesoscopic assumption. The term tumor cell loss rate indirectly involves insufficient and inadequate angiogenesis. In addition, the diffusion coefficient summarizes inter alia the microscopic chemotactic and haptotactic interactions of normal nerve fibers and tumor cells. In this framework, all biochemical and molecular mechanisms have been implicitly "summarized" and only their final outcome has "jumped" onto the upper cellular level through the use of more macroscopic parameters. This means that an adequate adaptation of the parameters ρ, *D*, and $G(t)$ to the particular molecular profile of the GBM of a patient could eventually lead to a high patient individualization of the model predictions. Summarizing several microscopic phenomena into a few parameter constitutes a pragmatic and usual approach which is partly dictated by the strongly multiscale character of tumor dynamics because tumor dynamics and in particular invasion are modeled primarily on the cellular level. The approach proposed in this article can be recruited to simulate the effect of treatment (such as radiotherapy, chemotherapy, immunotherapy, combined, and experimental therapies) in a rather gross way. The parameter $G(t)$ which describes the temporal profile of treatment can vary enormously depending on the treatment scheme administered.

To demonstrate the workflow of a possible clinical validation procedure, a clinical case/scenario is addressed. Using appropriate imaging data sets of real tumors for comparison with the model simulation results would be particularly useful. However, this is a difficult task due to a number of limitations including pertinent legislation. Nevertheless, use of appropriate imaging data has been made in this article. Significantly, the proposed approach could be applied to mathematically similar phenomena within the fields of physics, chemistry, and biology, such as chemical reactors, embryology, and, more generally, growth and differentiation of human tissue.

## Conclusions

A novel explicit numerical treatment of the Neumann boundary condition problem of glioma growth and infiltration into the surrounding inhomogeneous brain tissue has been proposed. Our approach has been based on the 3D reaction-diffusion equation solved by the finite-difference method and especially the Crank-Nicolson scheme in conjunction with the BiCG method. A series of numerical experiments has been conducted to study the behavior of the proposed treatment and to check its validity. Based on the *in silico* experimentation presented, the model has proved to satisfy several natural conditions including the blocking of tumor cell diffusion toward the skull without any artificial loss of glioma cells in the skull-brain barrier. A preliminary theoretical exploration suggests that a rough but nonetheless informative value of the doubling time may be calculated based on a homogeneous brain model for the same clinical context. The results obtained support the potential of the presented biomodel to serve as the main component of a continuous mathematics-based GBM oncosimulator. Following a future

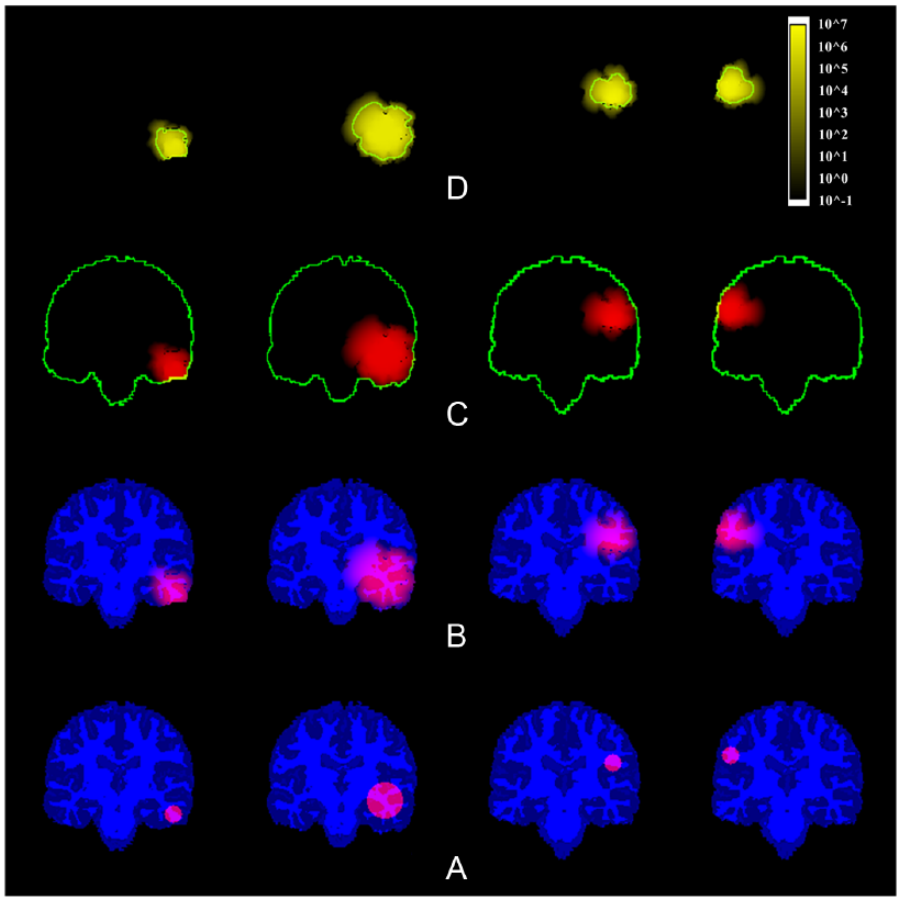


**Figure 20.** Schematic representation (coronal slice) of the growth of different cases of initial virtual glioblastoma. For simplicity and clarity reasons, only the brain is shown. (A) Four different cases of initial virtual glioblastoma. The threshold for tumor visualization has been taken to be equal to $1\,\text{cell/mm}^3$. In the panel columns, from left to right, the diameter of the spherical glioblastoma corresponds to 1.5, 3, 1.5, and 1.5 cm, respectively. (B) and (C) On the 180th simulated day, the tumor has diffused theoretically over the entire brain. (D) The outer green contour of the slices corresponds to the tomographically detectable tumor boundary at a detection level of $8000\,\text{cells/mm}^3$. The color bar corresponds to the tumor cell concentration scale considered (cells per $\text{mm}^3$).

thorough clinical validation, such oncosimulator could also be used as an individualized treatment planner through *in silico* experimentation and using the multiscale data of the patient. Given that in most cases GBM tumors are at least partly excised, the model could be used to simulate the response of the eventual tomographically imageable leftovers of the tumor surgical excision. It could also be used to study and quantify the possible natural history of a newly diagnosed GBM tumor.

## Acknowledgements

The authors duly acknowledge the constructive discussions with Norbert Graf, MD, University Hospital of Saarland, Germany; Stefaan Gool, MD, University Hospital of Leuven; and Dimitra Dionysiou, PhD, ICCS, NTUA, Greece.

## Author Contributions

GS and SG conceived and designed the experiments, analyzed the data, wrote the first draft of the manuscript, contributed to the writing of the manuscript, agree with manuscript results and conclusions, jointly developed the structure and arguments for the paper, and made critical revisions and approved final version. All authors reviewed and approved the final manuscript.

## REFERENCES

1. Ostrom QT, Gittleman H, Stetson L, Virk SM, Barnholtz-Sloan JS. Epidemiology of gliomas. *Cancer Treat Res*. 2015;163:1–14.
2. Guiou M, Pelloski C. Recent advances in the treatment of malignant gliomas and future directions. In: Thomas CR, ed. *Malignant Gliomas*. New York, NY: Demos Medical Publishing; 2012:190–191.
3. Barani IJ, Larson DA. Radiation therapy of glioblastoma. *Cancer Treat Res*. 2015;163:49–73.
4. Goffart N, Lombard A, Lallemand F, et al. CXCL12 mediates glioblastoma resistance to radiotherapy in the subventricular zone [published online ahead of print July 1, 2016]. *Neuro Oncol*. doi:10.1093/neuonc/now136.
5. Eikenberry SE, Sankar T, Preul MC, Kostelich EJ, Thalhauser CJ, Kuang Y. Virtual glioblastoma: growth, migration and treatment in a three-dimensional mathematical model. *Cell Prolif*. 2009;42:511–528.
6. Parker JJ, Dionne KR, Massarwa R, et al. Gefitinib selectively inhibits tumor cell migration in EGFR-amplified human glioblastoma. *Neuro Oncol*. 2013;15:1048–1057.
7. Giese A, Westphal M. Glioma invasion in the central nervous system. *Neurosurgery*. 1996;39:235–250.
8. Murray JD. *Mathematical Biology II: Spatial Models and Biomedical Applications*. 3rd ed. New York, NY: Springer-Verlag; 2003.
9. Swanson KR. Quantifying glioma cell growth and invasion in vitro. *Math Comput Model*. 2008;47:638–648.

10. Clatz O, Bondiau PY, Delingette H, et al. *Brain Tumor Growth Simulation* [Research report]. RR-5187. France: INRIA. https://hal.inria.fr/inria-00071401. Published 2004. Accessed March 15, 2016.
11. Clatz O, Sermesant M, Bondiau P-Y, et al. Realistic simulation of the 3-D growth of brain tumors in MR images coupling diffusion with biomechanical deformation. *IEEE Trans Med Imaging*. 2005;24:1334–1346.
12. Macklin P, Lowengrub JS. A new ghost cell/level set method for moving boundary problems: application to tumor growth. *J Sci Comput*. 2008;35:266–299.
13. Clatz O, Bondiau P, Delingette H, et al. *In silico* tumor growth: application to glioblastomas. In: Barillot C, Haynor DR, Hellier P eds. *Medical Image Computing and Computer-Assisted Intervention—MICCAI 2004*. Berlin, Germany: Springer, 2004;3217:337–345.
14. Becker S, Jungmann JO, Mang A, Buzug TM. An adaptive landmark scheme for modeling brain deformation in diffusion-based tumor growth. In: Dössel O, Schlegel WC eds. *World Congress on Medical Physics and Biomedical Engineering, September 7-12, 2009, Munich, Germany*. Berlin, Germany: Springer, 2010;25: 41–44.
15. McCorquodale P, Collela P, Johansen H. A Cartesian grid embedded boundary method for the heat equation on irregular domains. *J Computational Physics*. 2001;173:620–635.
16. Kansal AR, Torquato S, Harsh GR, Chiocca EA, Deisboeck TS. Simulated brain tumor growth dynamics using a three-dimensional cellular automaton. *J Theor Biol*. 2000;203:367–382.
17. Wise SM, Lowengrub JS, Frieboes HB, Cristini V. Three-dimensional multispecies nonlinear tumor growth—I. Model and numerical method. *J Theor Biol*. 2008;253:524–543.
18. Konukoglou E, Clatz O, Delingette H, Ayache N. Personalization to brain gliomas characterization and radiotherapy planning. In: Deisboeck T, Stamatakos G, eds. *Multiscale Cancer Modelling*, Boca Raton, FL: CRC Press; 2011:385–406.
19. Frieboes HB, Lowengrub JS, Wise S, et al. Computer simulation of glioma growth and morphology. *Neuroimage*. 2007;37:S59–S70.
20. Giatili S, Uzunoglu N, Stamatakos G. An explicit boundary condition treatment of a diffusion based glioblastoma tumor growth model. In: Proceedings of the 4th International Advance Research Workshop on *In Silico* Oncology Cancer Investigation; September 8-9, 2010; Athens, Greece. http://www.4th-iarwisoci.iccs.ntua.gr/. Accessed March 10, 2016.
21. Milotti E, Chignola R. Emergent properties of tumor microenvironment in a real-life model of multicell tumor spheroids. *PLoS ONE*. 2010;5:e13942.
22. Cruywagen G, Woodward D, Tracqui P, Bartoo G, Murray J, Alvord E. The modeling of diffusive tumors. *J Biol Syst*. 1995;3:937–945.
23. Woodward DE, Cook J, Tracqui P, Cruywagen GC, Murray JD, Alvord EC. A mathematical model of glioma growth: the effect of extent of surgical resection. *Cell Prolif*. 1996;29:269–288.
24. Burgess PK, Kulesa PM, Murray JD, Alvord EC. The interaction of growth rates and diffusion coefficients in a three-dimensional mathematical model of gliomas. *J Neuropathol Exp Neurol*. 1997;56:704–713.
25. Roniotis A, Manikis GC, Sakkalis V, Zervakis ME, Karatzanis I, Marias K. High-grade glioma diffusive modeling using statistical tissue information and diffusion tensors extracted from atlases. *IEEE Trans Inf Technol Biomed*. 2012;16:255–263.
26. Hogea C, Davatzikos C, Biros G. Modeling glioma growth and mass effect in 3D MR images of the brain. *Med Image Comput Comput Assist Interv*. 2007;10:642–650.
27. Stamatakos GS, Dionysiou DD, Zacharaki EI, Mouravliansky NA, Nikita K, Uzunoglu N. *In Silico* radiation oncology: combining novel simulation algorithms with current visualization techniques. *Proc IEEE*. 2002;90:1764–1777.
28. Dionysiou DD, Stamatakos GS, Uzunoglu NK, Nikita KS, Marioli A. A four-dimensional simulation model of tumour response to radiotherapy *in vivo*: parametric validation considering radiosensitivity, genetic profile and fractionation. *J Theor Biol*. 2004;230:1–20.
29. Stamatakos GS, Kolokotroni EA, Dionysiou DD, Georgiadi EC, Desmedt C. An advanced discrete state-discrete event multiscale simulation model of the response of a solid tumor to chemotherapy: mimicking a clinical study. *J Theor Biol*. 2010;266:124–139.
30. Stamatakos G. Multiscale cancer modeling. In: Deisboeck TS, Stamatakos GS, eds. *In Silico Oncology Part I: Clinically Oriented Cancer Multilevel Modeling Based on Discrete Event Simulation*. Boca Raton, FL: CRC Press; 2010:407–436.
31. Stamatakos GS, Georgiadi EC, Graf N, Kolokotroni EA, Dionysiou DD. Exploiting clinical trial data drastically narrows the window of possible solutions to the problem of clinical adaptation of a multiscale cancer model. *PLoS ONE*. 2011;6:e17594.
32. Stamatakos G, Dionysiou D, Lunzer A, et al. The technologically integrated oncosimulator: combining multiscale cancer modeling with information technology in the *in silico* oncology context. *IEEE J Biomed Health Inform*. 2014;18: 840–854.
33. Bauer S, May C, Dionysiou D, Stamatakos G, Buchler P, Reyes M. Multiscale modeling for image analysis of brain tumor studies. *IEEE Trans Biomed Eng*. 2011;59:25–29.
34. Stamatakos GS, Antipas VP, Uzunoglu NK. A spatiotemporal, patient individualized simulation model of solid tumor response to chemotherapy in vivo: the paradigm of glioblastoma multiforme treated by temozolomide. *IEEE Trans Biomed Eng*. 2006;53:1467–1477.
35. Giatili SG, Stamatakos GS. A detailed numerical treatment of the boundary conditions imposed by the skull on a diffusion–reaction model of glioma tumor growth. Clinical validation aspects. *Appl Math Comput*. 2012;218:8779–8799.
36. Steel G. *Basic Clinical Radiobiology*. London, England: Arnold; 2002.
37. Swanson KR, Bridge C, Murray JD, Alvord EC Jr. Virtual and real brain tumors: using mathematical modelling to quantify glioma growth and invasion. *J Neurol Sci*. 2003;216:1–10.
38. Swanson KR, Alvord EC, Murray JD Jr. Dynamics of a model for brain tumors reveals a small window for therapeutic intervention. *Discrete Cont Dyn: B*. 2004;4:289–295.
39. Sharma A, Shishodia MS, Reddy GB. Numerical simulation of inhomogeneous and nonlinear diffusion. *Phys Status Solidi*. 2006;243:1193–1204.
40. Fieremans E. *Validation Methods for Diffusion Weighted Magnetic Resonance Imaging in Brain White Matter* [PhD dissertation]. Faculty of Engineering, Ghent University; 2008. http://hdl.handle.net/1854/LU-891081. Accessed February 3, 2016.
41. Smith GD. *Numerical Solution of Partial Differential Equations: Finite Difference Methods*. 3rd ed. New York, NY: Oxford University Press; 1985.
42. Bradie B. *A Friendly Introduction to Numerical Analysis*. Boston, MA: Pearson International; 2006:246.
43. LeVeque RJ. *Finite Difference Methods for Ordinary and Partial Differential Equations: Steady-State and Time-Dependent Problems*. Philadelphia, PA: SIAM; 2007:35–37.
44. Harko T, Mak MK. A travelling wave solutions of the reaction-diffusion mathematical model of glioblastoma growth: an Abel equation based approach. *Math Biosci Eng*. 2015;12:41–69.
45. Gerlee P, Nelander S. Travelling wave analysis of a mathematical model of glioblastoma growth. *Math Biosci*. 2016;276:75–81.
46. Khan LA, Liu PL-F. An operator-splitting algorithm for the three-dimensional diffusion equation. *Numer Meth Part D E*. 1995;11:617–624.
47. Fedorov A, Beichel R, Kalpathy-Cramer J, et al. 3D slicer as an image computing platform for the quantitative imaging network. *Magn Reson Imaging*. 2012;30:1323–1341.
48. 3D Slicer. A multi-platform, free and open source software package for visualization and medical image computing. http://www.slicer.org/. Accessed May 1, 2015.
49. ImageJ. Image Processing and Analysis in Java. http://rsbweb.nih.gov/ij/. Accessed May 1, 2015.
50. Swanson KR, Alvord EC, Murray JD. A quantitative model for differential motility of gliomas in grey and white matter. *Cell Prolif*. 2000;33:317–329.
51. Baldock AL, Rockne RC, Boone AD, et al. From patient-specific mathematical neuro-oncology to precision medicine. *Front Oncol*. 2013;3:62.
52. Discussion Forum. How to solve the problem of negative concentration. http://www.comsol.com/community/forums/general/thread/29200/. Accessed July 26, 2015.
53. John V, Mitkova T, Roland M, Sundmacher K, Tobiska L, Voigt A. Simulations of population balance systems with one internal coordinate using finite element methods. *Chem Eng Sci*. 2009;64:733–741.
54. Stein AM, Demuth T, Mobley D, Berens M, Sander L. A mathematical model of glioblastoma tumor spheroid invasion in a 3D in vitro experiment. *Biophys J*. 2007;92:356–365.
55. Swanson KR, Alvord EC, Murray JD. Virtual brain tumors (gliomas) enhance the reality of medical imaging and highlight inadequacies of current therapy. *Br J Cancer*. 2002;86:14–18.
56. Alvord EC Jr, Shaw CM. Neoplasm affecting the nervous system in the elderly. In: Duckett S, ed. *The Pathology of the Aging Human Nervous System*. Philadelphia, PA: Lea & Febiger; 1991:210–281.